PHYSICAL REVIEW B **109**, 125421 (2024)

Prediction for an intrinsic ferrovalley semiconductor in a Janus 2*H*-CeBrCl monolayer with a high Curie temperature and perpendicular magnetic anisotropy

Yankai Chen, Xiaosong Zhao, and Yukai An[*]
School of Material Science and Engineering, Tianjin University of Technology, Tianjin 300384, China

(Received 28 September 2023; revised 3 March 2024; accepted 5 March 2024; published 20 March 2024)

Two-dimensional (2D) ferrovalley materials with intrinsic ferromagnetic ordering and spontaneous spin-valley splitting provide a great platform in nanoscale valleytronic devices. In this paper, the stability, mechanical, magnetic, transport, and valley properties of the Janus 2*H*-CeBrCl monolayer are predicted based on density functional theory calculations. The Janus 2*H*-CeBrCl monolayer exhibits an intrinsic ferromagnetic (FM) semiconductor character with a high Curie temperature (T_c) of 540 K, a large piezoelectric coefficient d_{11} of 2.95 pm/V, a robust perpendicular magnetic anisotropy (PMA), and a spontaneous valley polarization (ΔV) of 29.1 meV. Applying the in-plane biaxial strain from −6 to 6%, the 2*H*-CeBrCl monolayer still remains FM ground states, and the ΔV and d_{11} monotonically increase from −18.1 to 59.4 meV and from 1.56 to 4.03 pm/V, respectively. It is noted that a transition from PMA to in-plane magnetic anisotropy occurs at the tensile strain of 2%, which is due to the sign reversal contributed by the Ce-$d_{xy}/d_{x^2-y^2}$ orbitals. The investigations of electrical transport show that the effective mass of the hole is isotropic, while the effective mass of the electron is anisotropic for the 2*H*-CeBrCl monolayer, corresponding to mobilities of the hole and electron along the x direction of 111.6 and 83.2 cm^2 V^{-1} s^{-1}, respectively. Moreover, the valley-contrast Berry curvature $\Omega_z(k)$ and valley anomalous Hall effect can be clearly observed due to the breaking of time and space reversal symmetry in the 2*H*-CeBrCl monolayer. Overall, the Janus 2*H*-CeBrCl monolayer can be considered as an attractive 2D intrinsic ferrovalley material for nanoscale electronics and valleytronic devices.

DOI: 10.1103/PhysRevB.109.125421

I. INTRODUCTION

With the development of valley degrees of freedom, the local energy extremum (valley) of band structures attracts a great deal of interest [1–8]. As the ideal valley materials, two-dimensional (2D) hexagonal systems possess pairs of energy degenerate but inequivalent valleys at the K and K' points of the Brillouin zone [9–12], which can be regarded as pseudospins [13–15]. Additionally, due to the large separation of momentum space at the K and K' valleys, the valley carriers can be selectively manipulated by opposite chiral circularly polarized light [16–18]. However, the degenerated K and K' valleys limit their practical application in valleytronic devices. In order to effectively utilize the valley states, some methods are used to lift the valley polarization through breaking the time reversal symmetry, including circularly polarized light [19,20], transition metal (TM) doping [21,22], external field [23,24], and magnetic proximity effects [25,26]. Although these methods can create and lift valley polarization, they are not suitable for practical applications. For circularly polarized light it is not easy to precisely control the dynamic process. TM doping can cause a negative impact on electronic performance due to the additional magnetic scattering. The introduction of external field only lifts a very low valley polarization of about 0.1–0.2 meV/T. Magnetic substrates with magnetic proximity effects may cause lattice distortion and impurity energy bands. Therefore, it is urgent to search for materials that can generate spontaneous valley polarization, which is beneficial to the application of valleytronics.

Discovery of 2D ferrovalley materials provides new opportunity to create spontaneous valley polarization [27], which is due to the breaking of time reversal symmetry by intrinsic ferromagnetic ordering. So far, many 2D ferrovalley materials have been proposed, such as $2H-\mathrm{VSe}_2$ [28], 2*H*-VSSe [29], LaBr$_2$ [30], VSi$_2$P$_4$ [31], $2H-\mathrm{GdI}_2$ [32], TiVI$_6$ [33], and NbX_2 (X = S, Se) [34]. According to the Mermin-Wagner theorem [35], the long-range ferromagnetism is generally prohibited for the 2D systems due to the strong thermal fluctuations, while, in some systems with strong spin-orbit coupling (SOC) effect, its large magnetic anisotropy (MA) will suppress the thermal fluctuations and preserve the ferromagnetism, which has been confirmed in the CrI$_3$ monolayer (T_c = 45 K) [36]. Thus, the strong SOC effect and large MA character are important parameters to keep the ferromagnetic (FM) ordering in the 2D ferrovalley materials. Here, the electronic structure, valley states, and MA of the Janus 2*H*-CeBrCl monolayer are studied in detail based on density functional theory calculations. The 2*H*-CeBrCl monolayer is predicted as intrinsic ferromagnetic semiconductor with ΔV of 29.1 meV and high T_c of 540 K and large perpendicular magnetic anisotropy (PMA) of 52 μeV/Ce. The ΔV and magnetic anisotropy energy (MAE) monotonously increase with strain and a transition from PMA to in-plane magnetic anisotropy (IMA) character also occurs. Moreover, the valley anomalous Hall effect (VAHE) can be observed when

---

[*] ayk_bj@126.com

2469-9950/2024/109(12)/125421(10)

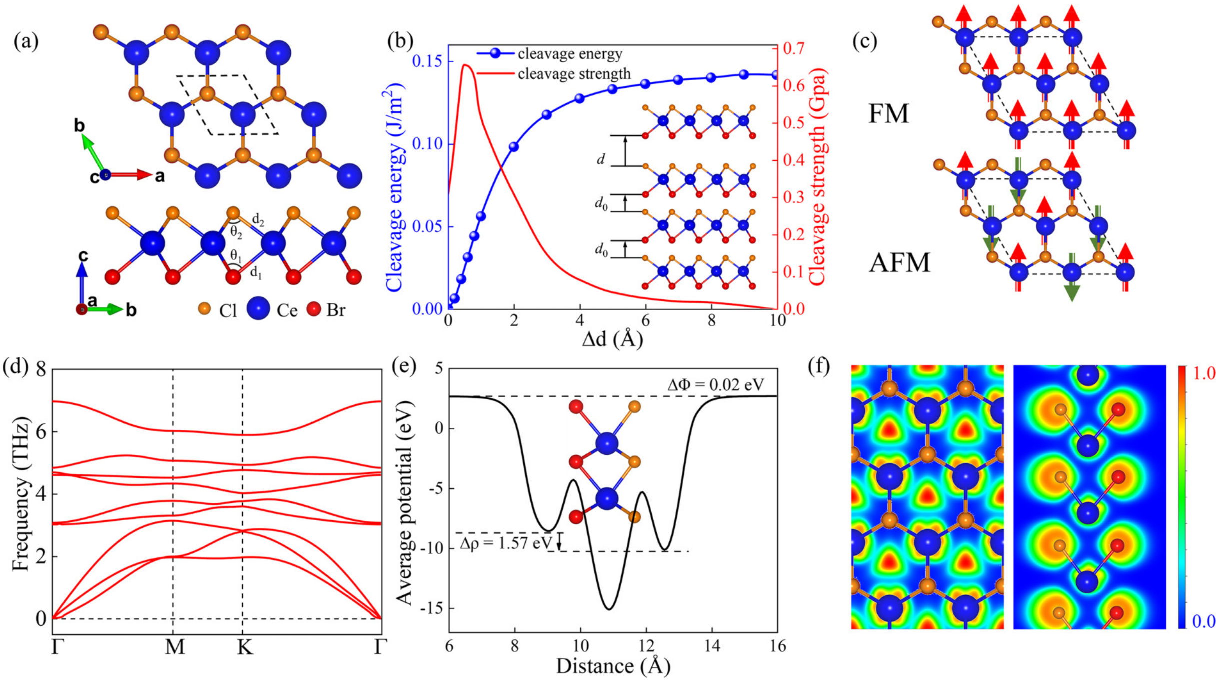

FIG. 1. (a) Top and side views of the optimized Janus 2H-CeBrCl monolayer. (b) The cleavage energy and cleavage strength as a function of separation distance ($\Delta d = d - d_0$), where d_0 and d are the equilibrium and unequilibrium van der Waals gap in the bulk crystal, respectively. The inset is the schematic of the exfoliation process. We show the (c) FM and AFM orderings, (d) phonon dispersion spectrum, and (e) average electrostatic potential of the 2H-CeBrCl monolayer. (f) The top and side views of the ELF image.

the in-plane electric field is applied in the Janus 2H-CeBrCl monolayer. Thus, the Janus 2H-CeBrCl monolayer can be considered as an attractive 2D intrinsic ferrovalley material for electronics and valleytronics.

II. COMPUTATIONAL METHODS

The first principles calculations have been performed with MEDEA using the *ab initio* total-energy and molecular dynamics package VASP [37,38]. The Perdew-Burke-Ernzerhof (PBE) method based on the generalized gradient approximation is used to treat the exchange-correlation functional and the electronic interaction is treated by the projector-augmented wave method [39,40]. The PBE+U calculation method is used to modify the strong correlation effects [41], where the on-site Coulomb interaction parameter $U = 7.47$ eV and exchange interaction parameter $J = 0.989$ eV are adopted for the 4f orbitals of the Ce atom [42]. The plane-wave energy cutoff and vacuum layer are set to 500 eV and 18 Å, respectively. The structure parameters are fully relaxed until the force and energy convergence are less than 0.01 eV/Å and 10^{-6} eV, respectively. The Brillouin zones of $12 \times 12 \times 1$ and $24 \times 24 \times 1$ k mesh Γ-centered Monkhorst-Pack grids are used for structural relaxation and electronic analyses. The T_c of the 2H-CeBrCl monolayer is estimated by the Monte Carlo simulation project MCSOLVER based on the classical Heisenberg model [43]. A $2 \times 2 \times 1$ supercell of the 2H-CeBrCl monolayer is used to calculate the phonon dispersion spectrum by the PHONOPY code [44,45] based on the density functional perturbation theory [46]. The electrical transport properties are performed with MEDEA ELECTRONICS by the BOLTZ-TRAP code version 1.2.2 [47]. The Berry curvature of the 2H-CeBrCl monolayer is calculated by WANNIER90 and VASPBERRY codes [48,49].

III. RESULTS AND DISCUSSIONS

Figure 1(a) displays the top and side views of the optimized 2H-CeBrCl monolayer with hexagonal lattice structure, in which the Ce atoms are sandwiched by the Cl and Br atoms. The optimized lattice constant a of the Janus 2H-CeBrCl monolayer is 4.045 Å (see Fig. S2 in Supplemental Material [60]), and the corresponding bond lengths of Ce-Br and Ce-Cl are $d_1 = 3.042$ Å and $d_2 = 2.912$ Å, respectively. The large bond length of Ce-Br is due to the larger atomic radius of the Br$^-$ ion (1.95 Å) compared with that of the Cl$^-$ ion (1.81 Å). Figure 1(b) shows the cleavage energy and cleavage strength as a function of separation distance Δd. The cleavage energy is calculated using the equation $E_{\text{cleavage}} = (E_d - E_{d_0})/S$, where S is the cleavage area of the material on the (001) plane, and E_{d_0} and E_d are the energies of bulk 2H-CeBrCl crystal with equilibrium interlayer distance d_0 and various interlayer distance d of the top layer, respectively. It can be seen that the energy of the system gradually increases and converges to 0.14 J/m^2 (cleavage energy) with the increase of separation distance ($\Delta d = d - d_0$). The cleavage energy of 0.14 J/m^2 is smaller than that of graphene (0.36 J/m^2) [50], suggesting that the 2H-CeBrCl monolayer can be easily mechanically exfoliated experimentally. The Bader charge analysis is calculated and listed in Table S1 in Supplemental Material [60]. The Ce atom loses 1.428 electrons while the Cl and Br atoms obtain 0.744 and 0.684 electrons, respectively. The valence state of the Ce atom is $6s^2 4f^1 5d^1$ and the electronic configuration of Ce becomes $4f^1 5d^1$ in the $2H$-CeBrCl monolayer due to the charge transfer from Ce to Br/Cl atoms. Thus, the magnetic moment of two μ_B/Ce atoms originates from the contributions of two spin-up Ce $5d$ and $4f$ orbitals. Generally, in the triangular prism crystal field of halogen atoms, the Ce-$5d$ orbital can split into three states, namely, a (d_{z^2}), e_1 (d_{xy}, $d_{x^2-y^2}$), and e_2 (d_{xz}, d_{yz}), which are displayed in Fig. S3(a) in Supplemental Material. The Ce d orbital resolved density of states are plotted in Fig. S3(b) in Supplemental Material [60]. Clearly, the spin-up e_1 state and the spin-down a and e_1 states are around the Fermi level (E_F). In addition, the orbital degeneracy of the e_2 state is also observed. Figure 1(c) displays the configurations of FM and antiferromagnetic (AFM) ordering for the $2H$-CeBrCl monolayer with the $2 \times 2 \times 1$ supercell. The calculated energies of FM and AFM ordering are -56.747 and -55.465 eV, respectively. Obviously, the energy of FM ordering is lower than that of AFM ordering, implying a stable FM ground state in the $2H$-CeBrCl monolayer. The calculated bond angles of Ce-Br-Ce and Ce-Cl-Ce are 83.3° and 87.9°, respectively, which are close to 90°. This further proves that the superexchange interaction dominates the stable FM ground state. On the other hand, the distance of nearest neighboring Ce-Ce atoms is large (4.045 Å), also resulting in a weak direct exchange interaction.

The cohesive energy of the $2H$-CeBrCl monolayer is defined as $E_{\mathrm{coh}} = (E_{\mathrm{Ce}} + \mathrm{E}_{\mathrm{Br}} + \mathrm{E}_{\mathrm{Cl}} - \mathrm{E}_{\mathrm{CeBrCl}})/3$, where E_{Ce}, E_{Br}, E_{Cl}, and E_{CeBrCl} are the energies of the isolated Ce, Br, Cl, atoms and $2H$-CeBrCl unit cell, respectively. The calculated E_{coh} in the Janus $2H$-CeBrCl monolayer is 4.36 eV per atom, which is larger than that in the $\mathrm{Cu_2Ge}$ monolayer (3.17 eV per atom) [51] and implies a stable structure. Figure 1(d) displays the phonon dispersion spectrum of the $2H$-CeBrCl monolayer. Clearly, the frequencies of all phonon modes within the Brillouin zone are positive, suggesting that the $2H$-CeBrCl monolayer with FM ground state is dynamically stable. The elastic tensor C is also calculated to investigate the mechanical stability [52], which is defined as

$$C = \begin{pmatrix} C_{11} & C_{12} & 0 \\ C_{21} & C_{22} & 0 \\ 0 & 0 & C_{66} \end{pmatrix} \tag{1}$$

The calculated values of C_{11}, C_{12}, and C_{66} are 35.19, 11.36, and 11.91 N/m, respectively. The calculated elastic constants C_{ij} satisfy the Born criteria of mechanical stability with $C_{11} > 0$ and $C_{11} - C_{12} > 0$, suggesting the good mechanical stability in the $2H$-CeBrCl monolayer [53]. Due to the hexagonal symmetry, the 2D Young's modulus $C^{2\mathrm{D}}$, shear modulus $G^{2\mathrm{D}}$, and Poisson ratio $\upsilon^{2\mathrm{D}}$ can be simply described as [54,55]

$$C^{2\mathrm{D}} = \frac{C_{11}^2 - C_{12}^2}{C_{11}}, \tag{2}$$

$$G^{2\mathrm{D}} = C_{66} = \frac{C_{11} - C_{12}}{2}, \tag{3}$$

$$\upsilon^{2\mathrm{D}} = \frac{C_{12}}{C_{11}}. \tag{4}$$

The calculated $C^{2\mathrm{D}}$, $G^{2\mathrm{D}}$, and $\upsilon^{2\mathrm{D}}$ are 35.52 N/m, 11.91 N/m, and 0.322, respectively. The $C^{2\mathrm{D}}$ is smaller than that of graphene (340 N/m) [56], suggesting that the $2H$-CeBrCl monolayer is suitable for the field of flexible materials. The different chemical compositions of two surfaces in the $2H$-CeBrCl monolayer can result in an inhomogeneous charge distribution and the formation of a built-in electric field at the interface. The change in electrostatic potential represents the difference in potential energy as it moves from one point to another in an electric field. The electrostatic potential along the z direction is calculated and displayed in Fig. 1(e). It is clear that the electrostatic potential is smaller on the Cl side than that on the Br side ($V_{\mathrm{Cl}} < V_{\mathrm{Br}}$, $\Delta\Phi = 0.02$ eV), corresponding to larger electronegativity of Cl atoms. Further, the asymmetric electrostatic potential on the two sides also exhibits a potential drop $\Delta\rho$ of 1.57 eV. Figure 1(f) plots the electron localization function to clarify the bonding character of the $2H$-CeBrCl monolayer. The obvious ionic bonding character can be observed with the electrons transferred from the Ce layer to the Br/Cl layer.

The MAE is a fingerprint of magnetic properties of 2D systems, which is calculated by comparing the energy difference of magnetic axis along the [001] and [100] direction considering SOC effect, namely, $\mathrm{MAE} = E_{[001]} - E_{[100]}$ [57]. The calculated MAE is -52 µeV, indicating a PMA character in the $2H$-CeBrCl monolayer. To investigate the spatial anisotropy of MAE, the MAE in the whole space under different polar angles θ and φ are calculated ($\mathrm{MAE}_\theta = E_\theta - E_{[001]}$). Figure 2(a) displays the angle dependence of MAE along with xy, xz, and yz planes. The MAE exhibits angle isotropy at the xy plane and strong angle anisotropy at xz and yz planes, which reaches a maximum value of 52 µeV under the polar angle of 90°. The strong PMA character is also proved in the MAE of the whole space in Fig. 2(b), namely, the MAE reaches a maximum value at the xy plane while it gradually decreases to zero when the magnetic axis turns to the z direction. As an important parameter of spintronics devices, T_c is calculated using the Heisenberg spin Hamiltonian, which can be expressed as [58,59]

$$H = -J \sum_{i,j} S_i S_j - D \sum_i \left(S_i^z\right)^2 \tag{5}$$

where S, J, and D are the spin vector, magnetic exchange parameter, and MAE, respectively. These parameters can be calculated considering SOC in $2 \times 2 \times 1$ supercells using the following equations:

$$E_{\mathrm{FM}} = E_0 - 6J|S|^2 - D|S|^2, \tag{6}$$

$$E_{\mathrm{AFM}} = E_0 + 2J|S|^2 - D|S|^2 \tag{7}$$

where E_0 is the ground state energy without the magnetic exchange interaction. $|S|$ can be considered as the total spin of the Ce atom (for details of the calculations, see Supplemental Material [60]). Therefore, J can be obtained by

$$J = \frac{E_{\mathrm{AFM}} - E_{\mathrm{FM}}}{8|S|^2}. \tag{8}$$

The calculated J value is 116 meV for the $2H$-CeBrCl monolayer. The magnetic moment and capacity of the Ce atom as a function of temperature for the $2H$-CeBrCl monolayer are calculated by Monte Carlo simulations and plotted in Fig. 2(c). The T_c value is predicted to be 540 K, which is recognized by the peak of capacity curves. The T_c for the $\mathrm{CrI_3}$ monolayer is

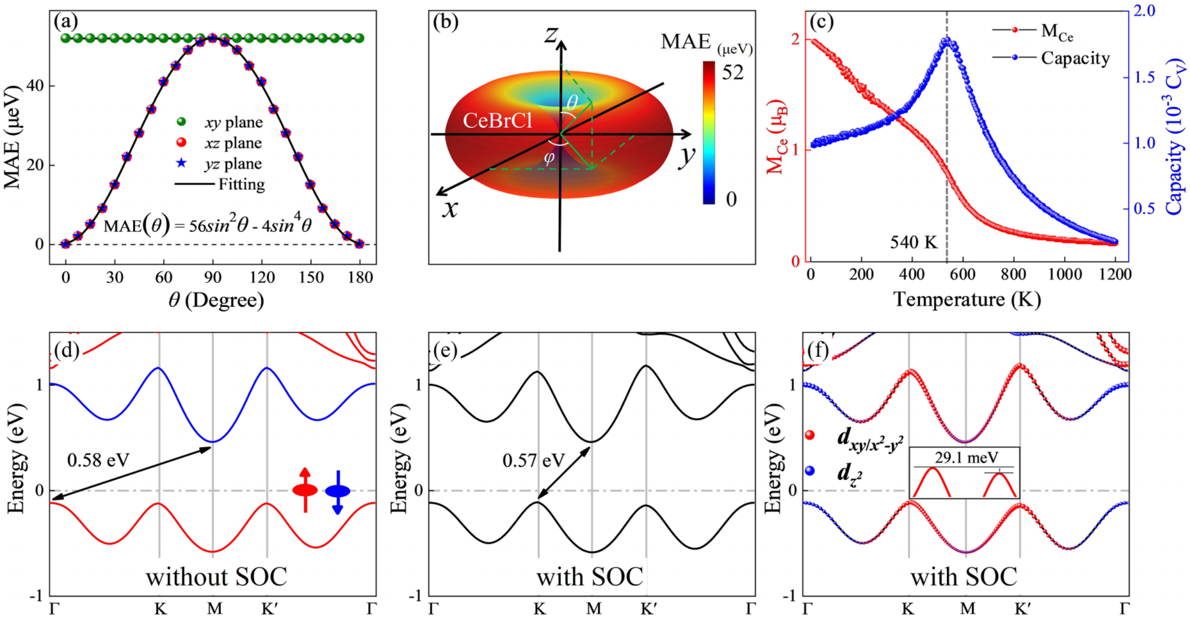

FIG. 2. The MAE along with (a) the *xy*, *xz*, and *yz* planes under the different polar angle (θ) and (b) the whole space for the 2*H*-CeBrCl monolayer. (c) The magnetic moment and capacity of the Ce atom as a function of temperature for the 2*H*-CeBrCl monolayer. We show the band structure (d) without SOC and (e) with SOC as well as (f) the Ce d-orbital projected band structure with SOC for the 2*H*-CeBrCl monolayer. The inset is an amplified view of K and K' valleys.

also calculated with the same method. The calculated value is 50 K, which well matches with the reported experimental value of 45 K [36].

Figure 2(d) displays the spin-resolved band structure of the 2*H*-CeBrCl monolayer. It is clear that the 2*H*-CeBrCl monolayer is a bipolar magnetic semiconductor with an indirect band gap of 0.58 eV, namely, the valence band maximum (VBM) is occupied by the spin-up electrons and the conduction band minimum (CBM) is occupied by the spin-down electrons. By applying the appropriate gate voltage, the E_F can pass through the VBM or CBM, which gives the 2*H*-CeBrCl monolayer a half-metallic character with 100% spin-polarized current. As shown in Fig. S4 in Supplemental Material [60], after adding 0.3 e of electrons and holes, the E_F passes through the original conduction band and valence band respectively, forming a 100% spin-polarized half metal. After the introduction of SOC, a spontaneous valley polarization of 29.1 meV can be observed due to the broken energy degeneracy at the K and K' valleys. Figure 2(f) plots the Ce d-orbital projected band structure with SOC. One can see that the K and K' valleys mainly originate from the contributions of Ce-$d_{xy}/d_{x^2-y^2}$ orbitals. In contrast, the Γ point is basically contributed by Ce-d_{z^2} orbital. Significantly, there exist no other bands near the E_F except for the VBM and CBM, which provides great convenience and possibility for modulating the valley polarization. Actually, for some nonmagnetic 2D systems, such as the 2*H*-WSSe monolayer, the space inversion symmetry breaking considering SOC effect does not generate the valley polarization character, which can only be achieved using the circularly polarized light or external magnetic field method by breaking the symmetry of time inversion. However, for the magnetic 2*H*-CeBrCl monolayer, the presence of intrinsic ferromagnetic ordering breaks the symmetry of time inversion, resulting in the occurrence of spontaneous valley polarization. Thus, the 2*H*-CeBrCl monolayer can be considered as an ideal ferrovalley material for potential applications of spintronic and valleytronic devices.

Applying in-plane biaxial strain is an effective method to tune the electronic properties of 2D systems. The in-plane biaxial strain is defined as $\varepsilon=(a-a_0)/a_0 \times 100\%$, where a and a_0 are the lattice parameters of the 2*H*-CeBrCl monolayer with and without strain, respectively. As shown in Fig. S5 in Supplemental Material [60], the stable FM ground state can be observed in the considered strain range from −6 to 6% for the 2*H*-CeBrCl monolayer. Figures 3(a) and 3(b) display the variation of band gap and valley polarization for the 2*H*-CeBrCl monolayer under various strains. The corresponding band structures of the 2*H*-CeBrCl monolayer under various strains are plotted in Fig. S6 in Supplemental Material. Clearly, as the strain increases from −6 to 6%, the band gap first increases and then decreases, and the maximum value occurs at the strain of 0%. In contrast, the valley polarization shows a monotonical increase trend with strain. Additionally, the valley polarization shows a negative value at the strain of −6%, suggesting an inversion character of valley polarization. To explain the monotonical increase of valley polarization, the dependences of the bond length d_1/d_2 and the bond angle θ_1/θ_2 on strains are plotted in Fig. S7 in Supplemental Material. With increasing strain from −6 to 6%, d_1 (from 3.01 to 3.10 Å), d_2 (from 2.88 to 2.97 Å), θ_1 (from 78.5° to 87.5°), and θ_2 (from 82.8° to 92.2°) show a monotonical increase trend. According to the Goodenough-Kanamori-Anderson rules [61], the increasing and approaching 90° for the θ_1 and θ_2 can enhance the superexchange interaction. On the other hand, the increase of bond length means the larger distance between the Ce atoms and weakens the direct exchange

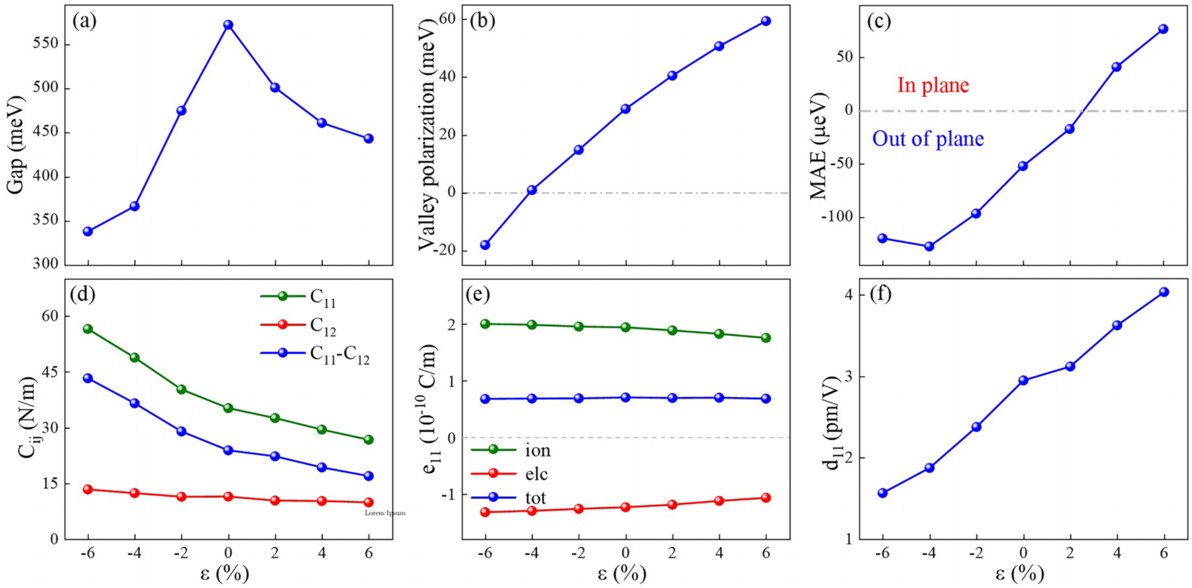

FIG. 3. The (a) band gap, (b) valley polarization, (c) MAE, (d) elastic constants C_{ij}, (e) piezoelectric tensor e_{11}, and (f) piezoelectric coefficient d_{11} as a function of strain ε for the 2H-CeBrCl monolayer.

interaction. Due to the competitive relationship between super- and direct-exchange interactions, the compression strain can weaken the FM coupling, while the tension strain increases the FM coupling, which results in a monotonical increase of valley polarization with strain.

The MAE under various strains is also studied and plotted in Fig. 3(c). The MAE monotonically increases with the increase of strain and a transition from PMA to IMA can be observed at the strain of 2% for the 2H-CeBrCl monolayer. Figure S8 in Supplemental Material [60] shows the atomic layer resolved MAE of the 2H-CeBrCl monolayer under various strains. the total MAE mainly originates from the contributions of Ce and Br atoms, especially for the Ce atom. The MAEs contributed by the Br and Cl atoms are both positive values, meaning an IMA character. In contrast, the MAE from the Ce atom shows the PMA character in the strain range from −6 to 2% and transforms into the IMA character in the strain range from 2 to 6%. Therefore, the changes in total MAE are mainly attributed to the changes in MAE of the Ce atom, which is consistent with the monotonical increase behavior of total MAE in Fig. 3(c). This also implies that the transition from IMA to PMA is mainly ascribed to the contribution of the Ce atom for the 2H-CeBrCl monolayer.

Due to the Janus character of the 2H-CeBrCl monolayer, there exist two independent in-plane piezoelectric coefficients d_{11} and out-of-plane piezoelectric coefficient d_{31}, which can be defined as [62]

$$d_{11} = \frac{e_{11}}{C_{11} - C_{12}}, \tag{9}$$

$$d_{31} = \frac{e_{31}}{C_{11} + C_{12}} \tag{10}$$

where e_{11} and e_{31} are the in-plane and out-of-plane piezoelectric tensor, respectively. The piezoelectric tensor is calculated with the orthorhombic supercell of the 2H-CeBrCl monolayer. The calculated e_{11} and e_{31} values are 0.7×10^{-10} and 0.041×10^{-10} C/m, respectively. e_{31} is much smaller than e_{11}, thus the subsequent discussions will only focus on the in-plane piezoelectric effect. e_{11} consists of the ionic part e_{11i} (1.944×10^{-10} C/m) and the electronic part e_{11e} (-1.242×10^{-10} C/m). Signs of the ionic and electronic parts are opposite and the piezoelectric tensor is dominated by the ionic part. The calculated d_{11} is 2.95 pm/V, which is larger than that of α quartz (d_{11}=2.3 pm/V). Furthermore, the elastic tensor C, piezoelectric tensor e, and in-plane piezoelectric coefficient d_{11} as a function of strain are plotted in Figs. 3(d)–3(f). Apparently, there is a significant decrease of C_{11} and a slight decrease of C_{12} within the strain range, which leads to a decrease of $C_{11} - C_{12}$. The positive values of C_{11}, C_{12}, and $C_{11} - C_{12}$ mean that the 2H-CeBrCl monolayer in the strain range can well satisfy the Born standard of mechanical stability criteria. For the piezoelectric tensor, the strain has little effect on e_{11} due to the slight changes in ionic and electronic parts. According to Eq. (9), $C_{11} - C_{12}$ monotonously decreases while e_{11} is almost unchanged with the increase of strain. Thus, the d_{11} shows an increasing trend with strain. The maximum and minimum values of d_{11} are 1.56 and 4.03 pm/V in the whole strain range, which indicates that the 2H-CeBrCl monolayer can maintain a good piezoelectric performance under the appropriate strain conditions and can be used in piezoelectric devices.

Figure 4 plots the Ce-d, Ce-p, and Br-p orbital-projected MAE of the 2H-CeBrCl monolayer at strains of −6, 0, and 6%. Obviously, the main contribution of MAE comes from the matrix elements differences between Ce-(d_{yz}, d_{z^2}), Ce-(d_{xy}, $d_{x^2-y^2}$), Ce-(p_x, p_y), and Br-(p_x, p_y) orbitals (for details of the orbital-projected MAE, see Supplemental Material [60]). The matrix element differences between Ce-(d_{yz}, d_{z^2}) orbitals keep a positive value in the whole strain range and increase with strain, indicating a contribution of IMA. Interestingly, the contribution of Ce-(d_{xy}, $d_{x^2-y^2}$) orbitals causes an obvious

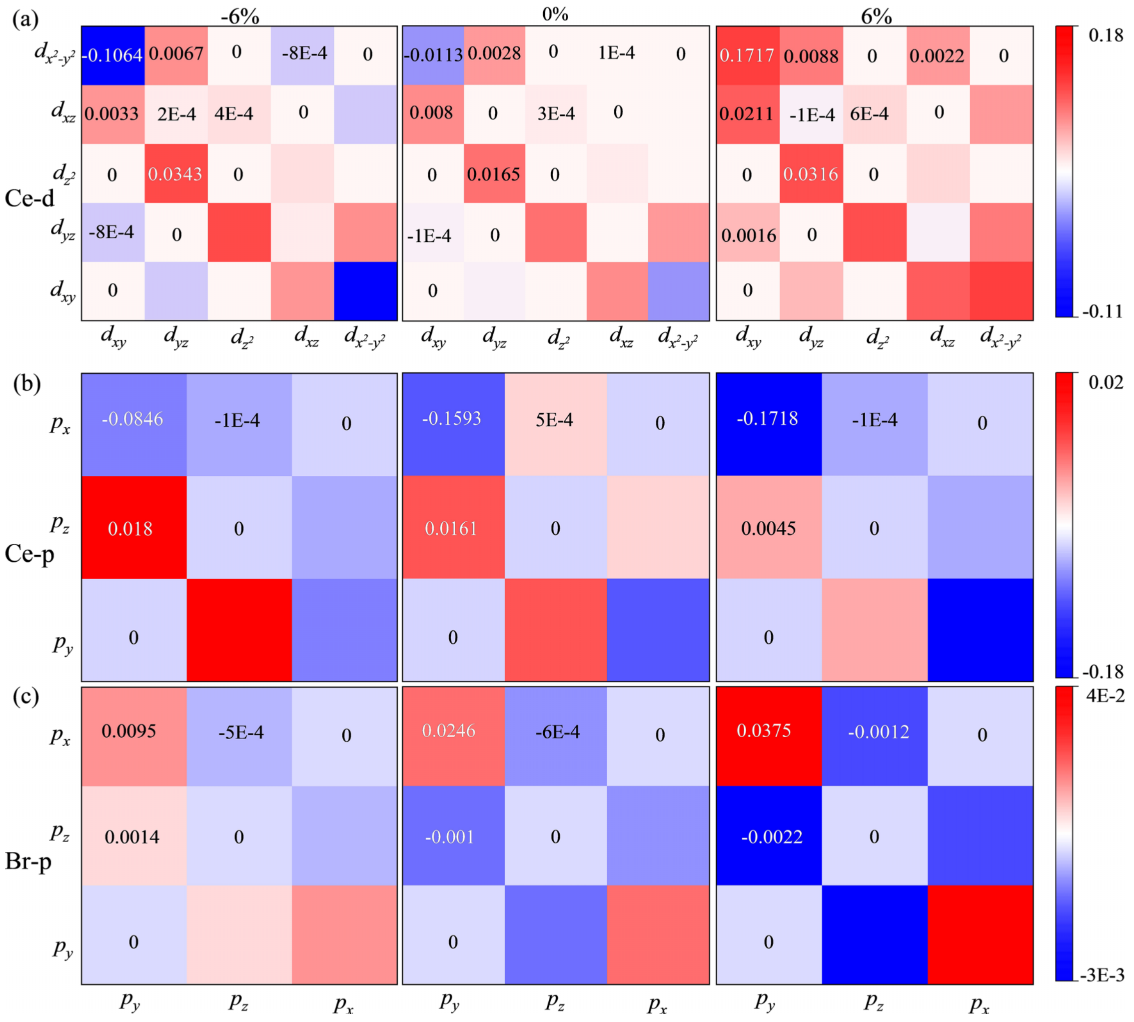

FIG. 4. (a) Ce-d, (b) Ce-p, and (c) Br-p orbital projected MAE under strains of −6, 0, and 6% for the Janus 2H-CeBrCl monolayer.

transition from the PMA to IMA character with the increase of strain. In addition, the Ce-(p_x, p_y) orbitals show a negative contribution of MAE, which is much larger than that from Br-(p_x, p_y) orbitals. Thus, the change of MAE from PMA to IMA can be attributed to the sign reversal of Ce-(d_{xy}, $d_{x^2-y^2}$) orbitals.

The 2H-CeBrCl monolayer exhibits semiconductor characteristics, thus the corresponding transport properties of the carrier need be investigated. The effective mass m^* of carriers can be defined as $m^*=\pm\hbar^2(\frac{d^2E_k}{dk^2})^{-1}$, where $\hbar$ and k represent the Plank constant and wave vector, respectively. As shown in Figs. 5(a) and 5(b), the angle dependence on m^* shows different characters. The effective mass of the hole exhibits isotropy with various angles, while the obvious anisotropy occurs in the effective mass of the electron. The calculated m^* of the hole is 0.63(m_0), while the minimum and maximum values of m^* reach 0.96 (m_0) and 8.77 (m_0) at the angle of 0° and 90° respectively. The three-dimensional band structures around the K point of the VBM and the M point of the CBM are calculated and plotted in Fig. S9 in Supplemental Material [60]. The result shows that the slope of the band structure around the K point of the VBM is isotropic, while that around the M point of the CBM is significantly anisotropic, which are consistent with the results of the effective mass related to the angle of holes/electrons.

The small effective mass at the K valley suggests the potential application for the electronic devices. The carrier mobility μ is also calculated and listed in Table I, which can be defined as [63] $\mu_x=\frac{e\hbar^3C}{K_BT(m_x^*)^{\frac{3}{2}}(m_y^*)^{\frac{1}{2}}E_d^2}$ and $\mu_y=\frac{e\hbar^3C}{K_BT(m_y^*)^{\frac{3}{2}}(m_x^*)^{\frac{1}{2}}E_d^2}$, where e, C, and E_d represent the electron charge, elastic constant, and deformation potential, respectively. The deformation potential is defined as the slope of energy changes in the VBM and CBM under small-scale strain

TABLE I. The carrier effective mass $m^*/(m_0)$ (m_0 means the rest mass of the free electron), elastic constant C (N/m), deformation potential E_d (eV), and estimated carrier mobility μ (cm^2 V^{-1} s^{-1}) of the Janus 2H-CeBrCl monolayer at room temperature.

Direction	Carrier type	m^*/m_0	C	E_d	μ
x axis	Electron	0.96	35.19	−1.801	83.2
	hole	0.63	35.19	−4.12	111.6
y axis	Electron	8.77	35.19	−1.801	9.11
	hole	0.63	35.19	−4.12	111.6

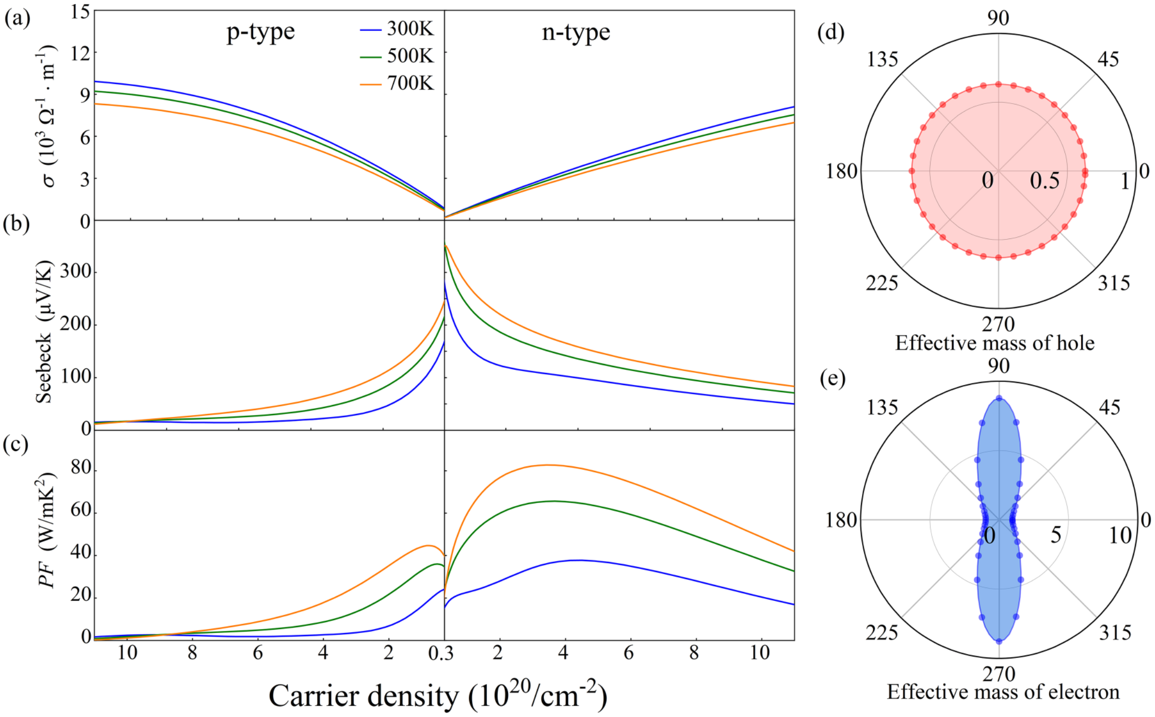

FIG. 5. The carrier density dependence on the (a) conductivity σ, (b) Seebeck coefficient S, and (c) power factor PF of the $2H$-CeBrCl monolayer along with the 0° direction at 300, 500, and 700 K, respectively. We show the angle dependence on the effective masses of (d) holes and (e) electrons of the $2H$-CeBrCl monolayer.

(within ±1%).The calculated μ_x values of the hole and electron are 111.6 and 83.2 $\mathrm{cm^2\,V^{-1}\,s^{-1}}$, respectively, which well matches with that of 2H-MoS$_2$ on the order of magnitude [64]. Additionally, the calculated μ_y values of the hole and electron are 111.6 and 9.11 $\mathrm{cm^2\,V^{-1}\,s^{-1}}$. The same μ_x and μ_y values of the hole are due to the isotropic effective mass.

The electrical transport properties of the $2H$-CeBrCl monolayer with p- and n-type conductivity are also investigated. Figures 5(a)–5(c) plot the carrier density dependence on conductivity σ, Seebeck coefficient S, and power factor PF at different temperatures of 300, 500, and 700 K. Clearly, σ decreases with the increase of temperature under the same carrier density and increases with the increase of carrier density under the same temperature, which is explained using the equation $\sigma = ne\mu$, where n and μ are the carrier density and mobility, respectively. As the temperature increases, the increasing lattice scattering shortens the relaxation time, resulting in a decrease of μ and σ. The Seebeck coefficient S can be used to characterize the magnitude of the Seebeck effect. Different from the σ, the absolute value of S increases with increasing the temperature and decreases with increasing the carrier density, which can be explained by $S = \frac{8\pi^2 k_B{}^2}{3eh^2} m^* T (\frac{\pi}{3n})^{2/3}$. Due to π, k_B, e, and h are all constant, which means that when the effective mass is the same, S is proportional to T and is inversely proportional to n. Power factor PF ($S^2\sigma$) also shows an increasing trend with temperature, as shown in Fig. 5(c). The opposite trend between parameters σ and S density means that the PF first reaches a maximum value and then decreases with the increase of carrier density.

The $2H$-CeBrCl monolayer display different properties with various doping types. Obviously, the σ of the p-type monolayer is higher than that of the n-type monolayer along the x direction. For example, the calculated σ with p type is 9286 $\Omega^{-1}\,\mathrm{m}^{-1}$ at 300 K with carrier density of $8 \times 10^{20}\ \mathrm{cm}^{-2}$, while it is 5971 $\Omega^{-1}\,\mathrm{m}^{-1}$ with n type at the same conditions. Since the μ with p type is larger than that with n type, as shown in Table I, the σ with p type is higher under the same carrier density. As for the Seebeck coefficient S, the S with n type is higher than that with p type. For example, the S (342 μV/K) with n type is larger than that (225 μV/K) with p type at 700 K with carrier density of $4 \times 10^{19}\ \mathrm{cm}^{-2}$, which can result in larger effective mass m^* of n-type carriers. For the power factor PF, the higher PF with n type can be attributed to the larger S with n type in the same situation. Thus, as a semiconductor, the $2H$-CeBrCl monolayer exhibits good electronic and thermoelectric performance.

The lack of mirror symmetry and time-reversal symmetry in the $2H$-CeBrCl monolayer can result in the existence of Berry curvature $\Omega_z(k)$ at the K and K' valleys, which is expressed by the following equation [65]:

$$\Omega_z(k) = -\sum_{n}\sum_{n\neq m} f_n \frac{2Im\,\langle\psi_{nk}|\,\hat{v}_x\,|\psi_{mk}\rangle\,\langle\psi_{mk}|\,\hat{v}_y\,|\psi_{nk}\rangle}{(E_{nk}-E_{mk})^2} \tag{11}$$

where $\hat{v}_x$ and $\hat{v}_y$ are the velocity operator along x and y directions, and ψ_{nk} is the wave function with energy eigenvalue of E_{nk}. Figures 6(a) and 6(b) display the $\Omega_z(k)$ of the $2H$-CeBrCl monolayer over the 2D Brillouin zone and along high symmetry lines, respectively. The maximum value of 6.61 bohrs^2 and the minimum value of -6.70 bohrs^2 of $\Omega_z(k)$

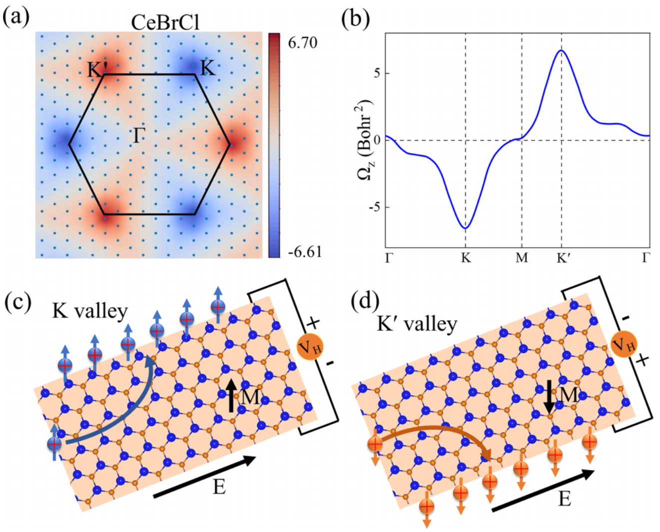

FIG. 6. Berry curvatures of the 2H-CeBrCl monolayer (a) in the 2D Brillouin zone and (b) along the high symmetry points. Schematic illustration of VAHE in the hole doped 2H-CeBrCl monolayer under in-plane electric field at the (c) K valley and (d) K' valley.

appears at the K and K' valleys, respectively. The $\Omega_z(k)$ of K and K' valleys exhibit different magnitudes with the opposite signs along the z direction, suggesting that the valley-contrasting character in the 2H-CeBrCl monolayer remains. The $\Omega_z(k)$ with nonzero value can be considered as an effective magnetic field when the in-plane electric field is applied, which brings the anomalous transverse velocity $v_\perp \sim E \times \Omega_z(k)$ for Bloch electrons [66]. Due to the energy difference between the K and K' valleys, the E_F can be effectively adjusted to the corresponding energy gap by an accurate hole doping, which makes the doped holes accumulate to the K' valley. Thus, the hole carriers should move to the edge of the sample under the in-plane electric field, which is called VAHE. Figures 6(c) and 6(d) display the schematic illustration of VAHE in the hole doped 2H-CeBrCl monolayer under in-plane electric field at the K/K' valley. When the magnetization of the 2H-CeBrCl monolayer is along the $+z$ direction, the spin-up holes at the K valley accumulate on one edge due to the $-\Omega_z(k)$ signal under the in-plane electric field. On the other hand, when the magnetization is along $-z$ direction, the valley polarization will flip and the spin-down holes at the K' valley accumulate on another edge due to the $+\Omega_z(k)$ signal. Thus, the 2H-CeBrCl monolayer can be applied to the valleytronic devices with VAHE as spin and valley filters, in which the transport carriers move in the horizontal plane by adding an in-plane longitudinal electric field.

IV. CONCLUSION

In conclusion, the stability, mechanical, magnetic, transport, and valley properties of the Janus 2H-CeBrCl monolayer are systematically investigated using first principles calculations. The 2H-CeBrCl monolayer displays high temperature (540 K) FM semiconductor characteristics with large PMA, d_{11}, and ΔV of 29.1 meV. The ΔV, MAE, and d_{11} monotonously increase with the increase of strain from -6 to 6%. Interestingly, a transition from PMA to IMA occurs at the tensile strain of 2%, which is due to the sign reversal from the contributions of Ce-d_{xy} and $d_{x^2-y^2}$ orbitals based on the d orbital-projected MAE. The calculation of electric transport shows that the σ of the p-type 2H-CeBrCl monolayer is larger than that of the n-type 2H-CeBrCl monolayer. The effective mass of the hole is isotropic, while the effective mass of the electron is anisotropic for the Janus 2H-CeBrCl monolayer. Additionally, the lack of mirror symmetry and time-reversal symmetry in the 2H-CeBrCl monolayer can result in the existence of valley contrast $\Omega_z(k)$ at the K and K' valleys, and the corresponding VAHE can be achieved by applying the appropriate external electric field. Overall, the Janus 2H-CeBrCl monolayer is a promising ferrovalley material for nanoscale electronics and valleytronic devices.

ACKNOWLEDGMENT

This work was supported by Natural Science Foundation of Tianjin City Municipal Science and Technology Commission, Grant No. 17JCYBJC17300.

---

[1] A. Soni and S. K. Pal, Valley degree of freedom in two dimensional van der Waals materials, J. Phys. D **55**, 303003 (2022).

[2] J. F. Sierra, J. Fabian, R. K. Kawakami, S. Roche, and S. O. Valenzuela, Van der Waals heterostructures for spintronics and opto-spintronics, Nat. Nanotechnol. **16**, 856 (2021).

[3] T. Gokmen, M. Padmanabhan, and M. Shayegan, Contrast between spin and valley degrees of freedom, Phys. Rev. B **81**, 235305 (2010).

[4] S. A. Wolf, D. D. Awschalom, R. A. Buhrman, J. M. Daughton, S. von Molnar, M. L. Roukes, A. Y. Chtchelkanova, and D. M. Treger, Spintronics: A spin-based electronics vision for the future, Science **294**, 1488 (2001).

[5] R. Rong, Y. Liu, X. C. Nie, W. Zhang, Z. H. Zhang, Y. P. Liu, and W. L. Guo, The interaction of 2D materials with circularly polarized light, Adv. Sci. **10**, 2206191 (2023).

[6] A. Sharan, S. Lany, and N. Singh, Computational discovery of two-dimensional rare-earth iodides: Promising ferrovalley materials for valleytronics, 2D Mater. **10**, 015021 (2023).

[7] J. R. Schaibley, H. Y. Yu, G. Clark, P. Rivera, J. S. Ross, K. L. Seyler, W. Yao, and X. D. Xu, Valleytronics in 2D materials, Nat. Rev. Mater. **1**, 16055 (2016).

[8] Y. Liu, Y. J. Gao, S. Y. Zhang, J. He, J. Yu, and Z. W. Liu, Valleytronics in transition metal dichalcogenides materials, Nano. Res. **12**, 2695 (2019).

[9] L. Qi, S. C. Ruan, and Y. J. Zeng, Review on recent developments in 2D ferroelectrics: Theories and applications, Adv. Mater. **33**, 2005098 (2021).

[10] F. Ding, S. L. Ji, S. S. Li, L. X. Wang, H. Wu, Z. F. Hu, F. Li, and Y. Pu, Prediction of intrinsic valley polarization in single-layer GdX$_2$ (X = Br, Cl) from a first-principles study, Phys. Status Solidi B **258**, 2100356 (2021).

[11] D. H. Kim, M. J. Shin, and D. Lim, Excitonic valley polarization and coherence in few-layer MoS_2, J. Korean Phys. Soc. **66**, 806 (2015).

[12] B. R. Zhu, H. L. Zeng, J. F. Dai, Z. R. Gong, and X. D. Cui, Anomalously robust valley polarization and valley coherence in bilayer WS_2, Proc. Natl. Acad. Sci. USA **111**, 11606 (2014).

[13] X. W. Zhao, B. Qiu, G. C. Hu, W. W. Yue, J. F. Ren, and X. B. Yuan, Transition-metal doping/adsorption induced valley polarization in Janus WSSe: First-principles calculations, Appl. Surf. Sci. **490**, 172 (2019).

[14] Q. Q. Zhang, X. T. An, and J. J. Liu, Electrical tuning of valley polarization in monolayer transition metal dichalcogenides, Phys. Rev. B **107**, 035411 (2023).

[15] A. Sharon and N. Singh, Intrinsic valley polarization in computationally discovered two-dimensional ferrovalley materials: LaI_2 and PrI_2 monolayers, Adv. Theor. Simul. **5**, 2100476 (2022).

[16] Q. P. Wu, Z. F. Liu, A. X. Chen, X. B. Xiao, H. Zhang, and G. X. Miao, Valley precession and valley polarization in graphene with inter-valley coupling, J. Phys.: Condens. Matter **29**, 395303 (2017).

[17] J. Liu, W. J. Hou, C. Cheng, H. X. Fu, J. T. Sun, and S. Meng, Intrinsic valley polarization of magnetic VSe_2 monolayers, J. Phys.: Condens. Matter **29**, 255501 (2017).

[18] H. C. Yang, M. Q. Song, Y. D. Li, Y. W. Guo, and K. Han, Ferromagnetism and valley polarization in Janus single-layer VSCl, Phys. E. **143**, 115341 (2022).

[19] S. Park, S. Arscott, T. Taniguchi, K. Watanabe, F. Sirotti, and F. Cadiz, Efficient valley polarization of charged excitons and resident carriers in molybdenum disulfide monolayers by optical pumping, Commun. Phys. **5**, 73 (2022).

[20] T. LaMountain, J. Nelson, E. J. Lenferink, S. H. Amsterdam, A. A. Murthy, H. Zeng, T. J. Marks, V. P. Dravid, M. C. Hersam, and N. P. Stern, Valley-selective optical stark effect of exciton-polaritons in a monolayer semiconductor, Nat. Commun. **12**, 4530 (2021).

[21] Y. C. Wu, T. Taniguchi, K. Watanabe, and J. Yan, Negative valley polarization in doped monolayer $MoSe_2$, Phys. Chem. Chem. Phys. **24**, 191 (2021).

[22] J. D. Zhou, J. H. Lin, H. Sims, C. Y. Jiang, C. X. Cong, J. A. Brehm, Z. W. Zhang, L. Niu, Y. Chen, and Y. Zhou, Synthesis of Co-Doped MoS_2 monolayers with enhanced valley splitting, Adv. Mater. **32**, 1906536 (2020).

[23] J. Holler, M. Selig, M. Kempf, J. Zipfel, P. Nagler, M. Katzer, F. Katsch, M. Ballottin, V, A. A. Mitioglu, and A. Chernikov, Interlayer exciton valley polarization dynamics in large magnetic fields, Phys. Rev. B **105**, 085303 (2022).

[24] Y. Zhang, K. Shinokita, K. Watanabe, T. Taniguchi, Y. Miyauchi, and K. Matsuda, Magnetic field induced inter-valley trion dynamics in monolayer 2D semiconductor, Adv. Funct. Mater. **31**, 2006064 (2021).

[25] Y. F. Lin, C. C. Zhang, L. X. Guan, Z. P. Sun, and J. G. Tao, The magnetic proximity effect induced large valley splitting in 2D InSe/FeI_2 heterostructures, Nanomaterials **10**, 1642 (2020).

[26] X. C. She, R. L. Zhang, J. Z. Zhao, D. X. Qi, Y. Zou, and R. W. Peng, Tunable valley polarization in Janus WSSe by magnetic proximity coupling to a CrI_3 layer, Phys. Chem. Chem. Phys. **23**, 18182 (2021).

[27] J. W. Chu, Y. Wang, X. P. Wang, K. Hu, G. F. Rao, C. H. Gong, C. C. Wu, H. Hong, X. F. Wang, and K. H. Liu, 2D polarized materials: Ferromagnetic, Ferrovalley, Ferroelectric materials, and related heterostructures, Adv. Mater. **33**, 2004469 (2021).

[28] W. Y. Tong, S. J. Gong, X. G. Wan, and C. G. Duan, Concepts of ferrovalley material and anomalous valley Hall effect, Nat. Commun. **7**, 13612 (2016).

[29] C. M. Zhang, Y. H. Nie, S. Sanvito, and A. Du, First-principles prediction of a room-temperature ferromagnetic Janus VSSe monolayer with piezoelectricity, ferroelasticity, and large valley polarization, Nano Lett. **19**, 1366 (2019).

[30] P. Zhao, Y. D. Ma, C. G. Lei, H. Wang, B. B. Huang, and Y. Dai, Single-layer $LaBr_2$: Two-dimensional valleytronic semiconductor with spontaneous spin and valley polarizations, Appl. Phys. Lett. **115**, 261605 (2019).

[31] X. Y. Feng, X. L. Xu, Z. L. He, R. Peng, Y. Dai, B. B. Huang, and Y. D. Ma, Valley-related multiple Hall effect in monolayer VSi_2P_4, Phys. Rev. B **104**, 075421 (2021).

[32] H. X. Cheng, J. Zhou, W. Ji, Y. N. Zhang, and Y. P. Feng, Two dimensional intrinsic ferrovalley GdI_2 with large valley polarization, Phys. Rev. B **103**, 125121 (2021).

[33] W. H. Du, Y. D. Ma, R. Peng, H. Wang, B. B. Huang, and Y. Dai, Prediction of single-layer $TiVI_6$ as a promising two dimensional valleytronic semiconductor with spontaneous valley polarization, J. Mater. Chem. C **8**, 13220 (2020).

[34] M. Zang, Yan, Y. D. Ma, R. Peng, H. Wang, B. B. Huang, and Y. Dai, Large valley-polarized state in single-layer NbX_2 ($X = S$, Se): Theoretical prediction, Nano Res. **14**, 834 (2021).

[35] N. D. Mermin and H. Wagner, Absence of ferromagnetism or antiferromagnetism in one- or two-dimensional isotropic Heisenberg models, Phys. Rev. Lett. **17**, 1133 (1966).

[36] D. R. Klein, D. MacNeill, J. L. Lado, D. Soriano, E. Navarro Moratalla, K. Watanabe, T. Taniguchi, S. Manni, P. Canfield, J. Fernández-Rossier, and P. Jarillo-Herrero, Probing magnetism in 2D van der waals crystalline insulators via electron tunneling, Science **360**, 1218 (2018).

[37] G. Kresse and J. Furthmüller, Efficiency of ab-initiototal energy calculations for metals and semiconductors using a plane-wave basis set, Comput. Mater. Sci. **6**, 15 (1996).

[38] G. Kresse and J. Furthmüller, Efficient iterative schemes for ab initio total-energy calculations using a plane-wave basis set, Phys. Rev. B **54**, 11169 (1996).

[39] J. P. Perdew, K. Burke, and M. Ernzerhof, Generalized gradient approximation made simple, Phys. Rev. Lett. **77**, 3865 (1996).

[40] P. E. Blöchl, Projector augmented-wave method, Phys. Rev. B **50**, 17953 (1994).

[41] S. L. Dudarev, G. A. Botton, S. Y. Savrasov, C. J. Humphreys, and A. P. Sutton, Electron-energy-loss spectra and the structural stability of nickel oxide: An LSDA+U study, Phys. Rev. B **57**, 1505 (1998).

[42] P. Larson, W. R. L. Lambrecht, A. Chantis, and M. van Schilfgaarde, Electronic structure of rare-earth nitrides using the LSDA+U approach: Importance of allowing 4f orbitals to break the cubic crystal symmetry, Phys. Rev. B **75**, 045114 (2007).

[43] L. Liu, X. Ren, J. Xie, B. Cheng, W. K. Liu, T. Y. An, H. W. Qin, and J. F. Hu, Magnetic switches via electric field in BN nanoribbons, Appl. Surf. Sci. **480**, 300 (2019).

[44] S. Baroni, S. de Gironcoli, A. Dal Corso, and P. Giannozzi, Phonons and related crystal properties from density-functional perturbation theory, Rev. Mod. Phys. **73**, 515 (2001).

[45] A. Togo and I. Tanaka, First principles phonon calculations in materials science, Scr. Mater. **108**, 1 (2015).

[46] X. Gonze and C. Lee, Dynamical matrices, Born effective charges, dielectric permittivity tensors, and interatomic force constants from density-functional perturbation theory, Phys. Rev. B **55**, 10355 (1997).

[47] G. K. H. Madsen and D. J. Singh, BoltzTraP: A code for calculating band-structure dependent quantities, Comput. Phys. Commun. **175**, 67 (2006).

[48] A. A. Mostofi, J. R. Yates, Y. S. Lee, I. Souza, D. Vanderbilt, and N. Marzari, WANNIER90: A tool for obtaining maximally localised wannier functions, Comput. Phys. Commun. **178**, 685 (2008).

[49] S. W. Kim, H. J. Kim, S. Cheon, and T. H. Kim, Circular dichroism of emergent chiral stacking orders in quasi-one-dimensional charge density waves, Phys. Rev. Lett. **128**, 046401 (2022).

[50] R. Zacharia, H. Ulbricht, and T. Hertel, Interlayer cohesive energy of graphite from thermal desorption of polyaromatic hydrocarbons, Phys. Rev. B **69**, 155406 (2004).

[51] L. M. Yang, I. A. Popov, A. I. Boldyrev, T. Heine, T. Frauenheim, and E. Ganz, Post-anti-van't Hoff–Le Bel motif in atomically thin germanium-copper alloy film, Phys. Chem. Chem. Phys. **17**, 17545 (2015).

[52] E. Cadelano, P. L. Palla, S. Giordano, and L. Colombo, Elastic properties of hydrogenated graphene, Phys. Rev. B **82**, 235414 (2010).

[53] M. Born and K. Huang, *Dynamical Theory of Crystal Lattices* (Clarendon Press, Oxford, 1954).

[54] S. D. Guo, J. X. Zhu, W. Q. Mu, and B. G. Liu, Possible way to achieve anomalous valley Hall effect by piezoelectric effect in a $GdCl_2$ monolayer, Phys. Rev. B **104**, 224428 (2021).

[55] E. Cadelano and L. Colombo, Effect of hydrogen coverage on the Young's modulus of graphene, Phys. Rev. B **85**, 245434 (2012).

[56] C. G. Lee, X. D. Wei, J. W. Kysar, and J. Hone, Measurement of the elastic properties and intrinsic strength of monolayer graphene, Science **321**, 385 (2008).

[57] K. Sheng, H. K. Yuan, and Z. Y. Wang, Monolayer gadolinium halides, GdX_2 ($X = F$, Cl, Br): Intrinsic ferrovalley materials with spontaneous spin and valley polarizations, Phys. Chem. Chem. Phys. **24**, 3865 (2022).

[58] B. Wang, X. W. Zhang, Y. H. Zhang, S. J. Yuan, Y. L. Guo, S. Dong, and J. L. Wang, Prediction of a two-dimensional high $T_c f$-electron ferromagnetic semiconductor, Mater. Horiz. **7**, 1623 (2020).

[59] K. Sheng, Z. Y. Wang, H. K. Yuan, and H. Chen, Two dimensional hexagonal manganese carbide monolayer with intrinsic ferromagnetism and half-metallicity, New J. Phys. **22**, 103049 (2020).

[60] See Supplemental Material at http://link.aps.org/supplemental/10.1103/PhysRevB.109.125421 for the details of Eqs. (6) and (7) and the orbital-projected MAE.

[61] P. W. Anderson, Antiferromagnetism: Theory of superexchange interaction, Phys. Rev. **79**, 350 (1950).

[62] L. Dong, J. Lou, and V. B. Shenoy, Large in-plane and vertical piezoelectricity in Janus transition metal dichalchogenides, ACS Nano **11**, 8242 (2017).

[63] H. Lang, S. Zhang, and Z. Liu, Mobility anisotropy of two-dimensional semiconductors, Phys. Rev. B **94**, 235306 (2016).

[64] B. Radisavljevic, A. Radenovic, J. Brivio, V. Giacometti, and A. Kis, Single-layer MoS_2 transistors, Nat. Nanotechnol. **6**, 147 (2011).

[65] D. J. Thouless, M. Kohmoto, M. P. Nightingale, and M. denNijs, Quantized Hall conductance in a two-dimensional periodic potential, Phys. Rev. Lett. **49**, 405 (1982).

[66] D. Xiao, M. C. Chang, and Q. Niu, Berry phase effects on electronic properties, Rev. Mod. Phys. **82**, 1959 (2010).